# Suppression of Metal Artifacts in CT Using a Reconstruction Procedure That Combines MAP and Projection Completion

Catherine Lemmens, David Faul and Johan Nuyts

***Abstract*—Metal implants such as hip prostheses and dental fillings produce streak and star artifacts in the reconstructed CT images. Due to these artifacts, the CT image may not be diagnostically usable. A new reconstruction procedure is proposed that reduces the streak artifacts and that might improve the diagnostic value of the CT images. The procedure starts with a MAP reconstruction using an iterative reconstruction algorithm and a multi-modal prior. This produces an artifact-free constrained image. This constrained image is the basis for an image-based projection completion procedure. The algorithm was validated on simulations, phantom and patient data, and compared with other metal artifact reduction algorithms.**

**Keywords: CT reconstruction, metal artifact, projection completion, iterative reconstruction**

## I. Introduction

Computed tomography (CT) is a routinely used imaging device in daily clinical practice. The combination of X-ray CT with positron emission tomography (PET) created the important new modality of PET/CT. One important application is tumor detection and staging. However, in the presence of high density objects, such as metals and concentrated oral contrast, the reconstruction algorithms used in daily clinical practice, like filtered back projection (FBP), give rise to streak and star artifacts. These artifacts impair the image quality of the CT images and thereby hamper the correct diagnosis. In radiation therapy, metal streak artifacts can shadow the tumor making tumor delineation very difficult. Furthermore, they will also influence the dose calculations. In PET/CT, one uses the CT images for the attenuation correction of the PET, therefore the artifacts may propagate into the PET images [1], [2].

Over the last thirty years, algorithms have been developed to reduce the metal artifacts. These metal artifact reduction (MAR) algorithms can be divided mainly into two classes: the projection completion based methods and the statistically based iterative methods. In the former case, the projections through the metal are treated as missing data. The incomplete data are then completed by interpolating between the measured data. Linear [3], [4] or polynomial [5], [6], [7] interpolation techniques can be used for this purpose. Projection completion in combination with filtering techniques has also been proposed [8], [9], [10]. In iterative reconstruction techniques the physics behind the metal artifacts is modeled. The most important causes of metal artifacts are noise, beam hardening, scatter, partial volume effects and aliasing [11]. Algorithms modeling the noise [12], [13] and the beam hardening [14], [15], [16] have been published. Recently, an algorithm combining projection completion with iterative reconstruction has also been proposed [17]. Other algorithms have been proposed like the one of [18] using wavelets.

The use of iterative reconstruction algorithms modeling the physics of the data acquisition is useful to deal with metal artifacts when the projection data through the metal still provide information. When the metal is too dense, it will stop all photons so that one is confronted with the so called exterior problem in tomography [19]. This problem has a unique solution, but it is severely ill-posed. This means iterative reconstruction algorithms will have trouble dealing with these data unless there is some kind of regularization.

In the case of the exterior problem, the use of projection completion is a valuable alternative. However, the use of interpolation techniques in the sinogram doesn't guarantee that the data are consistent, especially when multiple metal objects are present. Therefore, we propose to use an image-based projection completion: The missing data will be completed by forward projection of an image. We assume that if that image is sufficiently similar to the true distribution, these artificial data will be superior to those obtained by interpolation in the sinogram.

The MAR algorithm proposed in this paper combines the iterative reconstruction techniques with projection completion. A key step of our approach for reducing the metal artifacts and for restoring some of the diagnostic information, is the creation of an artifact-free constrained image. By applying strong constraints the formation of streak artifacts in the constrained image is prohibited. As a result, this image is not disturbed by typical metal artifacts, but it suffers from a reduced soft tissue contrast. The projection completion is then based on this constrained image rather than on a sinogram-based interpolation. To accelerate convergence, the constrained image will be given as an input image for the final reconstruction.

The design of this MAR algorithm was motivated by the results of initial experiments that were conducted to evaluate the effectiveness of metal artifact suppression by several

C. Lemmens and J. Nuyts are with the Dept. of Nuclear Medicine, K.U.Leuven, B-3000 Leuven, Belgium, (e-mail: catherine.lemmens@uz.kuleuven.be). D. Faul is with Siemens Medical Solutions, MI, Knoxville, TN, USA. This work was supported by the "Institute for the Promotion of Innovation through Science and Technology in Flanders (IWT-Vlaanderen)" and by Siemens Medical Solutions. 

iterative reconstruction techniques. In the next section these initial experiments will be discussed briefly before describing in detail the MAR algorithm and especially the Maximum-A-Posteriori (MAP) [13] procedure to obtain the constrained image. Several simulations and phantom measurements are described which contribute to the validation of the method. The MAR algorithm was also applied to patient data and in addition to that, a comparison was made with two other MAR algorithms.

## II. Initial experiment

An initial experiment was performed to evaluate the effectiveness for metal artifact suppression of the maximum-likelihood algorithm for transmission tomography (MLTR) [12] and of the iterative maximum-likelihood polychromatic algorithm for CT (IMPACT) [15], and to determine whether the metal projections provide useful information.

*1) Simulation:* A 2D dental head phantom (ellipse 200 x 140 mm) was defined as shown in fig. 1A. Four details (diameter 10 mm) with a contrast of 100 HU with respect to the soft tissue background were inserted in between the teeth and three amalgam dental fillings (3 disks with diameters 6, 7 and 9 mm) were inserted into the teeth. The simulated data were reconstructed using seven different approaches: FBP, MLTR initiated with a homogeneous image, MLTR initiated with the correct solution, MLTR initiated with the correct solution but ignoring the metal projections, MLTR initiated with a homogeneous image but ignoring the metal projections, and IMPACT started from a homogenous image and from the correct solution. Detailed information on the simulation of the data can be found in section IV-A.

*2) Results:* The first reconstruction was done with FBP, shown in fig. 1B. With normal gray-level windowing, the streak artifacts obscured almost all details in the image. The second reconstruction, shown in fig. 1C, used the MLTR algorithm which suffered from the metal streak artifacts but gave improved image quality when compared to FBP. In a third approach, the MLTR algorithm was used but instead of initiating the reconstruction with a homogeneous image, reconstruction was initiated with the correct solution. As can be seen in fig. 1D, the MLTR algorithm diverges away from the correct solution. In a fourth approach, MLTR reconstruction was again initiated with the correct solution, but the MLTR algorithm was set to ignore all the projections through the metal. As shown in fig. 1E, the MLTR algorithm stayed very close to the correct solution and suffers only from some small black spot artifacts around the metal inserts. For the last MLTR approach, the MLTR algorithm was initiated with a homogeneous image as in the second approach, but the projections through the metal were not used during reconstruction which resulted in the reconstruction shown in fig. 1F. The IMPACT reconstructions are shown in fig. 1G-H. They are very similar to the corresponding MLTR reconstructions (fig. 1C-D).

*3) Discussion:* The results of this simulation show that in the presence of metal objects, iterative reconstruction gives improved images over FBP reconstruction. However no visible differences were seen between the MLTR and the IMPACT

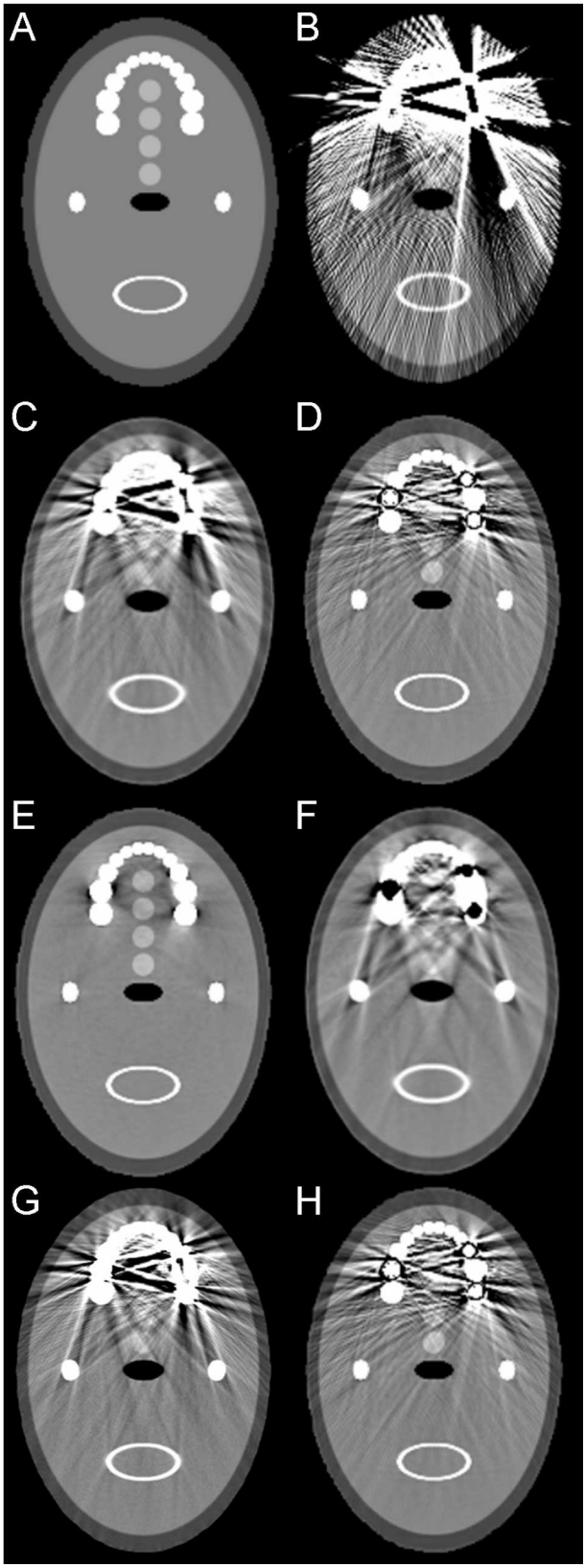


Fig. 1. Initial experiment using a head phantom with three dental fillings. A) The reference image, B) the FBP reconstruction, the MLTR reconstruction initiated from C) a homogeneous image, D) the reference image A, E) the reference image A and ignoring the metal projections, and F) a homogeneous image and ignoring the metal projections. The IMPACT reconstruction G) started from a homogeneous image, and H) started from the reference image. The window used is 500 HU centered at 0 HU.

reconstructions. This indicates that beam hardening is not the major cause of the metal artifacts. We think partial volume effects are the most important cause of the artifacts.

The results also show that when the metal projections are ignored, the likelihood does not have a well defined maximum and unregularized iterative reconstruction algorithms converge to a different solution which strongly depends on the image the reconstruction was started from. Full modeling of all physical effects during reconstruction was not considered for this work. As a result, MLTR and even IMPACT are not able to correctly handle the projections through the metal, and they perform better when these projections are not used.

These findings suggest that an artifact-free reconstruction could be obtained, when a good constrained image can be provided and the projections through the metal are ignored. However, in this experiment, reconstruction was initiated from the correct solution, something that in clinical practice can never be done. We found that if the constrained image is not similar enough to the correct reconstruction, then ignoring the metal projections still results in severe artifacts (black spots) around the ignored data region in the reconstruction. In the clinical data, these artifacts caused a great loss of detail in the surroundings of the metal and, moreover, such reconstructions are unsuitable for PET attenuation correction in PET/CT. To conclude, in the clinical context, using the metal projections gives rise to streak artifacts, not using them gives rise to black spot artifacts. One solution to this problem has been projection completion [3], [4], [5], [6], [7].

Based on these observations, a MAR algorithm is proposed that consists of four steps. In the first step, an initial reconstruction is performed with MLTR. We prefer to work with MLTR instead of IMPACT since, in this case, no benefit is seen from using IMPACT and since the computation times for IMPACT are much longer. In the second step, the initial reconstruction is segmented into three classes. For each class a prior is defined and based on these priors a MAP reconstruction is performed in order to obtain the constrained image. In the third step, this streak-free constrained image is then the basis for an image-based projection completion procedure. In the final step, MLTR is applied to compute the reconstruction from the completed projections. To accelerate this step, MLTR is started from the constrained image, not from the usual uniform image.

The core of the MAR algorithm is the combination of the creation of an artifact-free constrained image with MAP and completing the projections based on this constrained image. Therefore, the MAR algorithm presented here will be called MAPPC or Maximum-A-Posterior based Projection Completion for the rest of this paper. In the next section, the MAPPC algorithm is described step by step.

## III. The MAPPC algorithm

### A. First step: Initial reconstruction

The initial reconstruction is performed with MLTR [12]. The acquisition model is written as follows:

$$\widehat{y}_i = b_i \exp(-\sum_{j=1}^{J} l_{ij}\mu_j) \tag{1}$$

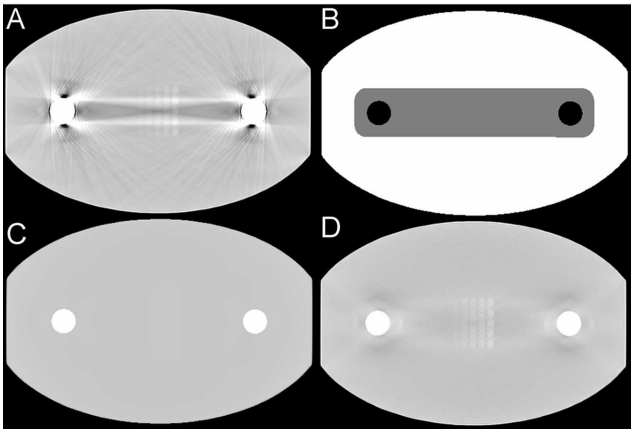


Fig. 2. The different steps of the MAPPC algorithm: A) The initial reconstruction, B) the label image, C) the constrained image, and D) the final reconstruction.

where $\widehat{y}_i$ is the expected number of detected photons given the image $\mu$, $b_i$ is the number of photons that would be detected in the absence of any absorber (the blank scan value) and $l_{ij}$ is the effective intersection length of projection line $i$ with pixel $j$. Assuming that $b_i$ is known and noise-free and that the measured transmission scan $y$ is subject to Poisson noise, the log-likelihood function becomes [20]:

$$L(y|\mu) = \sum_{i=1}^{I}(y_i \ln \widehat{y}_i - \widehat{y}_i - \ln y_i!) \tag{2}$$

with $y_i$ the measured data. Equation 1 can be inserted into equation 2, which is then optimized for the image $\mu$. In [12], a gradient ascent algorithm is derived to maximize the objective function, which leads to the following update step:

$$\mu_j^{n+1} = \mu_j^n + \frac{\sum_{i=1}^{I} l_{ij}(\widehat{y}_i - y_i)}{\sum_{i=1}^{I} l_{ij}[\sum_{h=1}^{J} l_{ih}]\widehat{y}_i} \tag{3}$$

This is the MLTR algorithm. In the case of metal artifacts and truncation, MLTR reconstructions will be superior to FBP. During FBP reconstruction all projections receive the same weight, whereas with MLTR, the projections through metal are appropriately assigned a lower weight [21], resulting in fewer artifacts. To obtain the initial image, the reconstruction is accelerated by using a gradually decreasing number of subsets [22] (iterations $\times$ subsets: $1\times580$, $1\times58$) which is approximately equivalent to 638 iterations of the unaccelerated MLTR algorithm. Figure 2A shows an initial reconstruction.

### B. Second step: MAP procedure to obtain constrained image

The following describes how a good constrained image is obtained by incorporating some *a-priori* knowledge in the iterative algorithm. In a patient, it is *a-priori* known which pixel values to expect because the pixel values represent the attenuation values of the human tissues. This knowledge can be represented with an absolute intensity prior [23], [24]. This prior tends to assign each pixel value to one of the modes of the prior. The most obvious modes to choose are the attenuation coefficients $\mu$ of air, fat tissue, soft tissue and

$$\mu_j^{n+1} = \mu_j^n + \frac{\sum_{i=1}^{I} l_{ij}(\widehat{y}_i - y_i) + \beta_G \frac{\partial}{\partial \mu_j}(\ln p_G(\mu)) + \beta_M \frac{\partial}{\partial \mu_j}(\ln p_M(\mu))}{\sum_{i=1}^{I} l_{ij}[\sum_{h=1}^{J} l_{ih}]\widehat{y}_i - \beta_G \frac{\partial^2}{\partial \mu_j^2}(\ln p_G(\mu)) - \beta_M \frac{\partial^2}{\partial \mu_j^2}(\ln p_M(\mu))} \tag{4}$$

bone (and some additional modes if there is lung tissue in the reconstructed image). The intensity priors are defined to behave as a Gaussian function with mean $\mu_i$ and standard deviation $\sigma_i$. By using a multi-modal prior in combination with a Markov Gibbs smoothing prior [24], [25], an image free of streak artifacts can be produced.

The reconstruction of the constrained image consists of the following steps:

1) Segmentation of the initial reconstruction into tissue classes based on thresholding.
2) Definition of an absolute intensity prior for each class in combination with a Gibbs Markov prior.
3) MAP reconstruction based on the defined priors to obtain the constrained image.

In the following each of these steps is described in more detail.

*1) Thresholding and defining the label image:* The initial reconstruction needs to be segmented into three classes for which different multi-modal priors will be defined. The segmented image will be called the label image; a label of 0, 1 or 2 will be assigned to the pixels belonging to the different classes. Label 2 contains all pixels belonging to the body of the patient. Label 1 contains all pixels within 2, which are likely to be affected by metal streak artifacts. Pixels labeled 0 belong either to air or to metal, these pixels can be reconstructed without using a prior. The attribution of a specific label to a pixel will be based on the pixels' attenuation value and on its location with respect to the metal.

In order to obtain the label image, two thresholds are applied to the initial reconstruction. First, the initial image is thresholded ($10^{-3}$ cm$^{-1}$) for all patient pixels and, when applicable, the patients' bed. These pixels will be assigned the label 2. Second, the initial image is thresholded for metal pixels. The threshold currently used is 0.8 cm$^{-1}$ ($\simeq$ 3071 HU), which is almost twice the linear attenuation value of cortical bone.

All pixels located in the convex hull defined by the metallic object(s) are assigned the label 1. The area of label 1 obtained in this way is further expanded by a predefined amount. This expansion was for a typical CT reconstruction (512×512) taken equal to 25 pixels. In this way, most of the pixels suffering from the metal dark band streak and star artifacts will be assigned the label 1.

Finally, the metal pixels will be assigned the label 0. All (air) pixels outside the patients body are also assigned the label 0. Figure 2B shows such a label image, (pixels with label 2 are white, pixels with label 1 are grey and pixels with label 0 are black).

*2) Defining the multi-modal priors:* For each label, a corresponding absolute intensity prior is defined. For label 2, containing most of the patient, a multi-modal prior is defined which has the modes air, fat, soft tissue and bone. For label 1, the vicinity of the metal, only the modes soft tissue and bone are used. Air is not included as a mode, because we do not want any black spots or streaks, which are common artifacts in the surroundings of the metal, in the constrained image. The multi-modal priors of label 2 and 1 are also combined with a Markov smoothing prior. For label 0, which contains the metals and the area around the patient, no prior is defined. We do not care which values the MLTR reconstruction assigns to the metal pixels because after the MAP reconstruction, the metal pixels will be replaced by the values of a less dense object. Also, we hope that in this way any inconsistency in the data will be accumulated at the location of the metal pixels during the reconstruction. MLTR is very good at reconstructing the air region, so no prior is assigned to this region.

*3) MAP reconstruction:* For the MAP reconstruction, two priors are combined: an absolute intensity prior which acts on individual pixels and a Markov Gibbs prior which acts locally and ensures local smoothness. The multi-modal prior is based on the label image as described above. The MAP objective function has the following form:

$$\Phi(\mu) = L(y|\mu) + \beta_M \ln p_M(\mu) + \beta_G \ln p_G(\mu) \tag{5}$$

where $\mu$ is the attenuation image, $y$ is the measured transmission data, $L(y|\mu)$ is the log-likelihood given in equation (2), $p_M(\mu)$ is a multi-modal prior distribution with weight $\beta_M$ and $p_G(\mu)$ is a Markov Gibbs prior with weight $\beta_G$. The objective function (eq. 5) is maximized using the gradient ascent algorithm described in [24]. This leads to the update step described by eq. 4.

The multi-modal prior distribution $p_M(\mu)$ is defined as a combination of Gaussians with mean $\mu_i$ and standard deviation $\sigma_i$ as described in [24]. The standard deviation $\sigma_i$ determines the weight that is given to each mode $\mu_i$. The lower the standard deviation, the more a pixel will be attracted towards the mean value of that mode. The prior is obtained by defining the gradient of its logarithm as a piecewise linear function, introducing additional points $t_i$ in the interval $[\mu_i, \mu_{i+1}]$:

$$\begin{aligned} \frac{\partial p_M(\mu|\mu_i, i=1..I)}{\partial \mu} &= \frac{\mu - t_{i-1}}{\sigma_i^2} \quad \text{if} \quad t_{i-1} < \mu \leq \frac{t_{i-1}+\mu_i}{2} \\ &= -\frac{\mu - \mu_i}{\sigma_i^2} \quad \text{if} \quad \frac{t_{i-1}+\mu_i}{2} < \mu \leq \frac{\mu_i + t_i}{2} \\ &= \frac{\mu - t_i}{\sigma_i^2} \quad \text{if} \quad \frac{\mu_i + t_i}{2} < \mu \leq t_i \end{aligned} \tag{6}$$

with $t_0 = -\infty$ and $t_I = \infty$. If $t_i$ is not in the center of the interval $[\mu_i, \mu_{i+1}]$ then more pixels will feel the attraction of one of the modes. For example, if $t_i$ is closer to the mode $\mu_i$ then more pixels in the interval $[\mu_i, \mu_{i+1}]$ will feel the attraction of mode $\mu_{i+1}$. For label 2 the intersection points were chosen in the middle of two modes. For label 1, the surroundings of the metal, the intersection points were chosen in such a way that three times more pixels were attracted to the soft tissue mode than to the bone mode in the range $[\mu_{soft}, \mu_{bone}]$.

The logarithm of the Markov Gibbs prior $p_G(\mu)$ can be written as follows:

$$\ln p_G(\mu) = -\sum_{j=1}^{J}\sum_{h=1}^{J} w_{jh} V(\mu_h - \mu_j) \tag{7}$$

where $w_{jh}$ is inversely proportional to the distance between pixels $j$ and $h$, $w_{jh}$ is zero if $h \notin N_j$, with $N_j$ the set of neighbors of pixel $j$. $V$ is the potential function which we choose to be the Huber function [26]:

$$V(\mu) = \begin{cases} \frac{\mu^2}{2\delta^2} & \text{for } |\mu| \leq \delta \\ \frac{|\mu| - \delta/2}{\delta} & \text{for } |\mu| \geq \delta \end{cases} \tag{8}$$

where $\delta$ is a positive constant, which was set to 0.033 cm$^{-1}$. This value was derived on a trial and error basis. For more details on the implementation of the Huber and the multi-modal prior, we refer to [24].

To tune the weight $\beta_M$, which is the most critical parameter for the MAP reconstruction, we started with a low value and increased it until the constrained image didn't show the dark band streak artifact anymore in between two metals and until all fine streak artifacts disappeared. The constrained image then looked as a segmented image. However, sometimes small "islands" of wrongly segmented pixels remained, which could be caused by the non-convexity of the multi-modal prior. Therefore, the weight $\beta_G$ of the Huber prior was increased until these "islands" were gone in the image. For the multi-modal prior, the standard deviation of each mode also needed to be set. The standard deviations are used to determine the relative weight for each mode, the global weight is tuned with $\beta_M$. The standard deviations of the air, fat tissue and bone mode were taken 15 times higher than the soft tissue mode.

For this MAP-reconstruction, the initial image serves as an input image and the MAP-reconstruction is obtained with 115 iterations accelerated with subsets (iterations $\times$ subsets: 2$\times$29, 2$\times$20, 1$\times$10, 1$\times$5, 1$\times$2). By including this prior information, the MAP reconstruction is forced toward a reconstruction that is streak-free and that has no black spots near the metal. Figure 2C shows such a constrained image.

### C. Third step: Projection completion

The metal pixels in the constrained image are replaced by pixel values of 0.8 cm$^{-1}$. That is, the original metal is replaced by a less dense object with the same shape as the metal. By choosing this high value, it is still possible to identify the metal region after the final reconstruction and the metal projections will still be assigned a lower weight during the final MLTR reconstruction. Then, this slightly modified constrained image is forward projected to form the "artificial" sinogram. In fig. 3A-B, the original and the artificial sinograms are shown, with a piece of their profile (C-D) for one view indicated by the line in the sinograms.

In the second step of the MAPPC procedure, the metal pixels were identified. By setting these metal pixels to one and all other pixels to zero, a binary image of the metal is created. By forward projection of this metal image, the corresponding projections of the metal in the original sinogram data can be identified. These metal projections in the original data are now replaced by the corresponding projections of the artificial sinogram. The transition between the original data and the replaced data should be smooth in order to avoid introducing artifacts. However, when simply replacing the metal projections in the original data with the corresponding projections of the artificial data, one can create discontinuities as is shown in fig. 3E. Such discontinuities give rise to streak artifacts in the reconstructions. To ensure a continuous transition between the two datasets, a modification of the metal projections in the artificial sinogram is made as follows. For each view, the values of the points neighboring the metal values are determined, both in the artificial data as well as in the original data. These values will be denoted by $O_L$ and $O_R$ for the original data, and by $A_L$ and $A_R$ for the artificial data. The subscripts $L$ and $R$ represent respectively the left and right neighboring point. The differences $D_L = O_L - A_L$ and $D_R = O_R - A_R$ and the number of detectorpoints $N$ in between $L$ and $R$ are determined. Each row of the metal projections of the artificial sinogram is modified by adding the following to the metal projections values:

$$S_i = D_L + i\frac{(D_R - D_L)}{N+1} \text{ with } i = 1..N \tag{9}$$

In this way, any discontinuities can be removed as shown in fig. 3F. With this procedure, one creates a sinogram in which the corrupted metal projections are replaced by the projections of a dense object.

### D. Fourth step: Final reconstruction

The final reconstruction using the projection completed data is done with MLTR using 667 iterations accelerated with subsets (iterations $\times$ subsets: 1$\times$580, 5$\times$58, 1$\times$29). A smoothed version of the constrained image, where the metal pixels were replaced by 0.8 cm$^{-1}$, is given as input image for this reconstruction. Figure 2D shows the final result.

### E. Reducing reconstruction time

The MAPPC algorithm needs three iterative reconstructions: the initial reconstruction, the MAP reconstruction and the final reconstruction. In a clinical setting, analytical reconstruction algorithms are preferred over iterative reconstruction since the latter is very time consuming and thus clinically impractical with the equipment available today. As mentioned before, the crucial steps of the MAPPC algorithm are the MAP reconstruction to obtain the constrained image and the projection completion step. Although MLTR has been used for the other two reconstructions, we found that similar results can be obtained with FBP instead of MLTR. This will be shown throughout the next sections, where results of both reconstruction algorithms will be presented.

## IV. Experiments

In order to evaluate the MAPPC algorithm, several experiments were conducted. In this section, we describe two computer simulation studies and one phantom measurement. Two patient studies were also selected to assess the usefulness of the algorithm on clinical data.

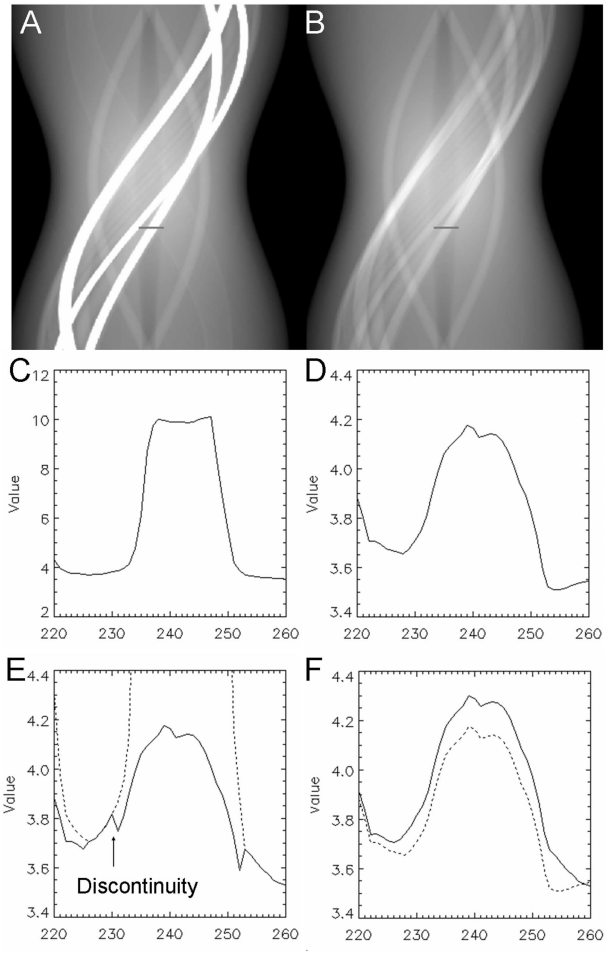


Fig. 3. Sinogram and profiles for the simulated head phantom. A) The original sinogram, B) the artificial sinogram, C) profile through the original data, D) profile through the artificial data, E) profile through the projected dataset when no compensation for discontinuity is applied (the dotted line represents the profile through the original data), and F) profile through the projected dataset when compensation for discontinuity is applied (the dotted line represents the profile through the artificial data). The profile's location is indicated by the line in the sinograms.

### A. Simulations

A hip phantom with two hip prostheses and a dental head phantom with three dental fillings were simulated using the 2D simulator described in [11]. The simulator takes into account the finite size of the detectors and the focal spot, and the view smoothing due to gantry rotation. A fan beam acquisition was simulated using 672 detectors and 1160 projection angles over 360°. The distance from the focus to the center of the FOV was 570 mm and the distance between the focus and the detector was 1040 mm. These parameters correspond to the central slice geometry of a Sensation 16 CT scanner (Siemens). The spectrum of the X-ray tube (at 120 kVp) of the Sensation 16 scanner was used to simulate the beam hardening effect. The spectrum information was obtained from the manufacturer. The spectrum is very similar to the spectrum described in [15]. A constant value was added to each pixel value of the transmission sinogram $y_i$, to simulate the contribution of scatter [27]. After simulation, the fan beam sinograms were rebinned to parallel beam data [28]. Reconstructions were performed with 512x512 pixels.

*1) Hip phantom:* A 2D hip phantom (dimensions 320x 210 mm) was defined as shown in fig. 4A. In the center of the phantom, a grid of 5x5 disks was inserted with each disk having a diameter of 7.5 mm. The disks have an increased CT number with respect to the soft tissue background varying between 10 and 50 in steps of 10 HU. Around each hip prosthesis, 4 disks (diameter 7.5 mm) were inserted with an increased CT number of 45 HU with respect to the background. To serve as a reference, a simulation was done without any metal and afterwards two titanium hip prostheses (circles with a diameter of 25 mm) were inserted and a second simulation was performed. Again, the images before and after MAPPC will be visually compared and difference images will be shown.

*2) Head phantom:* This experiment used the same phantom as described in the initial experiment. To serve as a reference, a simulation was first done without any metal, and afterwards the three amalgam dental fillings were inserted and a second simulation was done. The images before and after MAPPC were visually compared, and the CT numbers of the four inserts and eight other regions of interest (ROI), drawn in the soft tissue background, were calculated.

### B. Phantom measurement

The phantom measurement was acquired on the CT part of a Biograph16 (Siemens Medical Solutions, Knoxville, TN) PET/CT scanner. The CT data were acquired at 120 kVp and 140 mAs with a slice thickness of 3 mm, using an 18 mm table feed per rotation and a rotation time of 0.5 s. In order to apply the MAPPC algorithm, the raw CT data were exported from the system enabling off-line reconstruction with our software. The "raw" CT data obtained from the scanner underwent the standard corrections of the scanner, including a dark signal correction, the log-conversion, converting the measured intensities to the integrals of attenuation coefficients, beam hardening correction, spectral response correction, and the gain correction.

The 3D cone beam CT sinograms were rebinned to a 2D parallel beam configuration. In order to apply MLTR to the CT-data, an arbitrary noise-free blank scan of $10^5$ photons per detector pixel was defined. The transmission scan was calculated as $y_i = b_i \exp(-r_i)$, where $b_i$ is the blank scan value for detector element $i$, $r_i$ is the "raw" CT-value and $y_i$ the computed transmission value.

For the phantom measurement, module CTP404 of the CATPHAN phantom (The Phantom Laboratory) was used. Two cylindrical amalgam fillings - contained in a plexiglas cylinder with a diameter of 12 mm - were placed at the location of the air holes of the CATPHAN phantom. The diameters of the two fillings were respectively 3 and 5 mm. The images before and after MAPPC were visually compared and six equally sized ROIs were drawn in order to compare the CT number from the different reconstruction methods.

### C. Patient studies

Two patient studies were selected to assess the usefulness of the MAPPC algorithm on clinical data. The first patient had

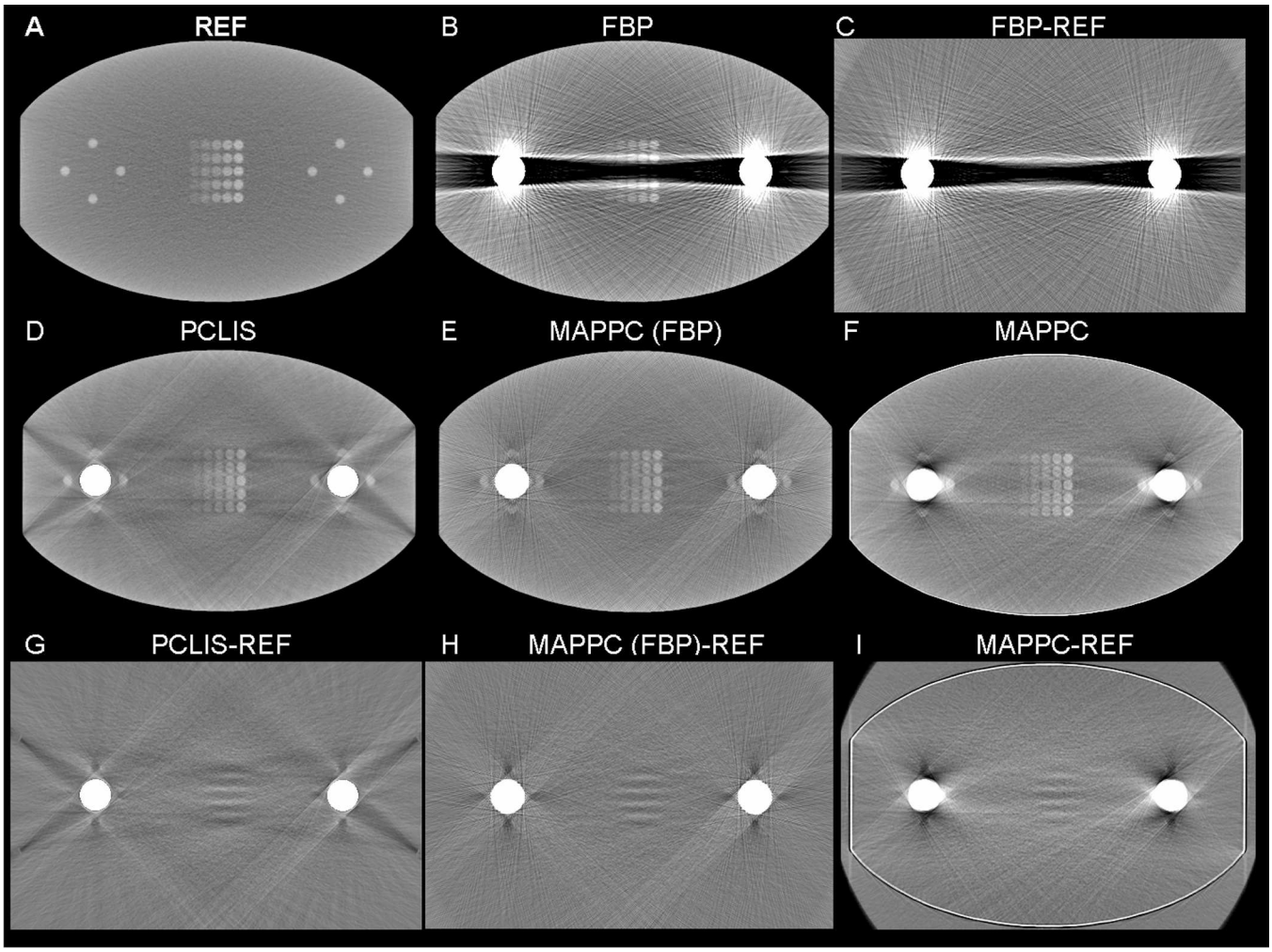


Fig. 4. The reconstructions of the simulated hip phantom. The window used was 200 HU centered at 0 HU. A) Without metal inserts reconstructed with FBP, with metal inserts reconstructed with B) FBP, D) PCLIS, E) MAPPC using FBP for initial and final reconstruction, and F) MAPPC . Difference images are shown for the reconstructions done with C) FBP, G) PCLIS, H) MAPPC with initial and final reconstruction done with FBP, and I) MAPPC.

a double hip prosthesis, the second one had several dental fillings. The patients were scanned on the same PET/CT system described above.

### *D. Comparison with projection completion based on interpolation*

All the results obtained with the MAPPC algorithm in the simulations, phantom measurement and patient studies, have been compared to the standard method commonly used to suppress the metal artifacts: the MAR algorithm proposed by Kalender et al. [4]. This is a projection completion method based on a linear interpolation in the sinogram (PCLIS). In the rest of the paper, the method of [4] will be referred to as PCLIS. The phantom measurement and the patient data were also reconstructed with the MAR method developed by Mahnken et al. [6]. This MAR method makes use of a polynomial (or multiple) interpolation in the sinogram and will be referred to as PCMIS in the rest of this paper. The developers of the algorithm made an implementation of their algorithm for data from a Siemens 16-slice CT scanner, which was made available to us.

## V. Results

### *A. Simulations*

*1) Hip phantom:* Figure 4 shows the reconstructions before and after projection completion. Visual evaluation shows that the band streak artifact is suppressed and that the grid of details in between the hip prostheses and the details around the hip prostheses become visible. Some residual black spot artifacts remain near the hip prostheses in the MAPPC reconstruction. From the difference images, it is clear that MAPPC and PCLIS yield a similar quantitative accuracy near the details in the center of the phantom. The MAPPC reconstruction was also done using FBP for the initial and the final reconstruction which is shown in fig. 4E. This reconstruction doesn't show an underestimation of the values around the hip prostheses.

*2) Head phantom:* Figure 5 shows the reconstructions before and after projection completion. Visual evaluation shows that with the MAPPC algorithm the metal artifacts are suppressed and that details become more visible than with the PCLIS method. Nevertheless, the MAPPC image is not totally artifact-free. Performing the final reconstruction with MLTR or with FBP gives very similar results. Figure 6 shows

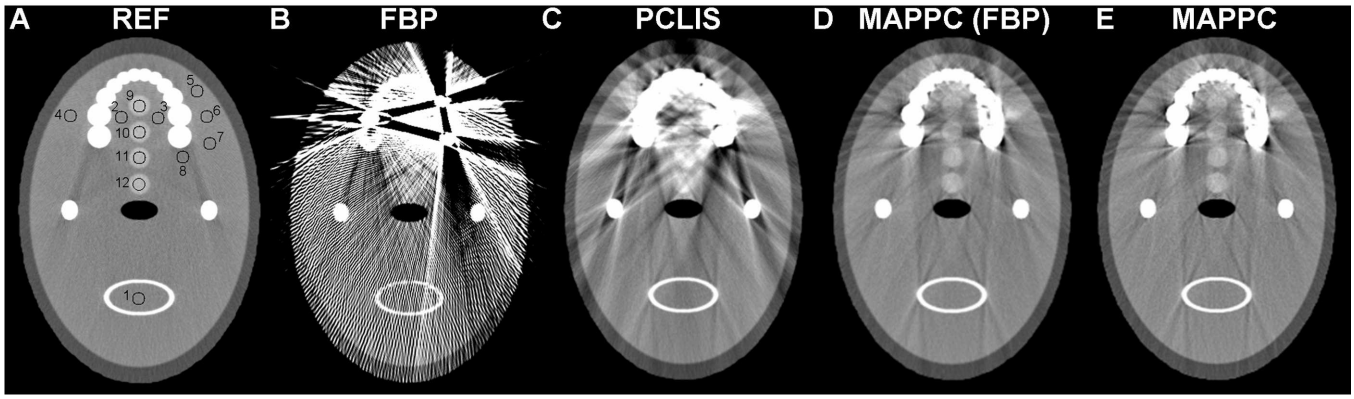


Fig. 5. The reconstructions of the simulated dental head phantom. The window used was 500 HU centered at 0 HU. A) FBP reconstruction of the simulation without metal inserts with the 12 ROIs used in the analysis. Reconstructions of the simulation with three dental fillings: B) FBP, C) PCLIS, D) MAPPC with the final reconstruction done with FBP, and E) MAPPC .

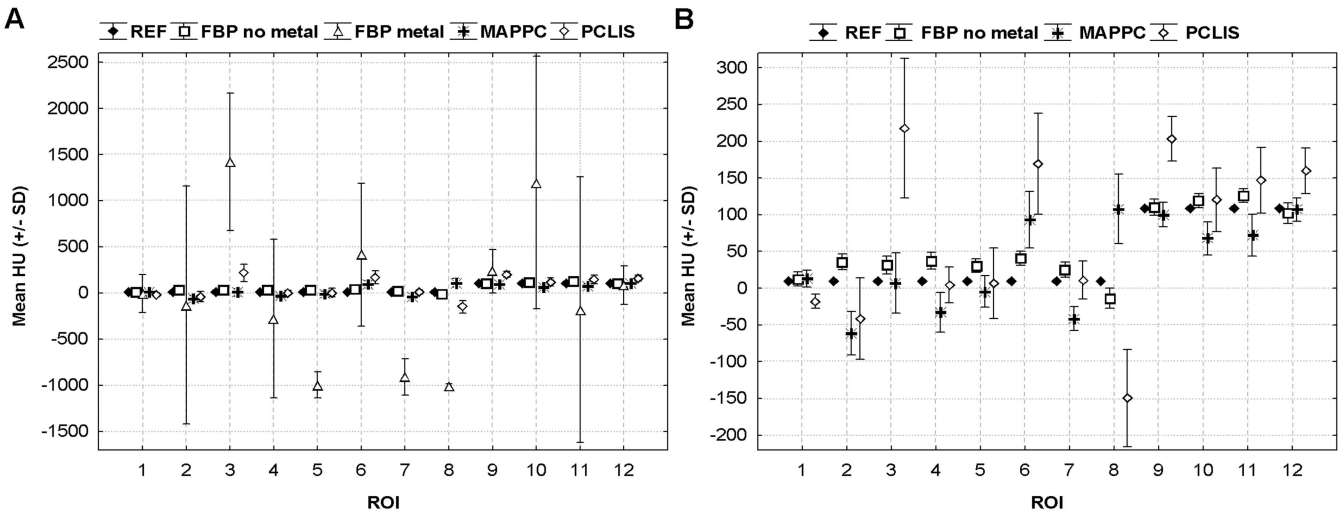


Fig. 6. The mean CT number and standard deviation (SD) of each ROI for the dental head phantom. Plot A gives the CT number from the reference image (REF), the FBP reconstruction of the simulation without the metal, and the FBP, MAPPC and PCLIS reconstruction of the simulation with metal. Plot B does not include the results from the FBP reconstruction when metal was present so that the differences between the other methods can be shown in more detail.

both the mean CT number of the details between the teeth and the other ROIs (all shown in fig. 5A) for the different reconstructions. It can be seen that in the presence of the amalgam dental fillings, the CT number of the ROIs under consideration deviate significantly from their reference value when FBP was used. When the reconstruction was performed with the MAPPC algorithm, the CT number of the ROIs were closely brought back to their original values.

### *B. Phantom measurement*

Figure 7 shows the FBP reconstructions of the measurement of the CTP404 module with and without the metal inserts, the MAPPC reconstruction and the PCLIS and PCMIS reconstruction. Figure 7 shows that the dark streak artifact visible in the FBP reconstruction disappears with all MAR algorithms. However, all MAR reconstructions still suffer from some artifacts. Six ROIs of equal size were drawn which are shown in fig. 7A. The mean CT number and standard deviation for each ROI in each reconstruction is given in table I. There is a great variation of the CT numbers within one ROI for the FBP reconstruction in the presence of the metal inserts. The mean CT numbers, however, don't deviate much from the values of the FBP reconstruction without the metal inserts except for ROI 6 which was drawn through the dark streak artifact. With all MAR algorithms the mean CT number of ROI 6 was restored and the variation on the CT number was reduced in each ROI.

| | FBP no metal | FBP with metal | MAPPC | PCLIS | PCMIS |
|---|---|---|---|---|---|
| ROI 1 | 943 ± 6 | 911 ± 63 | 934 ± 28 | 889 ± 11 | 933 ± 9 |
| ROI 2 | -181 ± 6 | -162 ± 34 | -172 ± 11 | -174 ± 8 | -188± 7 |
| ROI 3 | -90 ± 8 | -90 ± 15 | -86 ± 12 | -89 ± 7 | -98 ± 7 |
| ROI 4 | -31 ± 8 | -32 ± 46 | -36 ± 13 | -37 ± 10 | -44 ± 10 |
| ROI 5 | 345 ± 9 | 326 ± 16 | 338 ± 12 | 331 ± 9 | 339 ± 11 |
| ROI 6 | 99 ± 9 | 24 ± 169 | 98 ± 13 | 96 ± 9 | 93 ± 9 |

TABLE I
THE TABLE SHOWS THE MEAN CT NUMBER (HU) AND THEIR STANDARD DEVIATION FOR THE 6 ROIS OF THE CATPHAN PHANTOM MEASUREMENT.

Instead of using MLTR for the initial and final reconstruction, one can use FBP which is shown in fig. 7E. As can be seen, the use of FBP results in some fine streaks artifacts originating in the metallic objects.

### C. Patient studies

Figure 8 shows the reconstructions of a patient with two hip prostheses. PCLIS, PCMIS and MAPPC give a good reduction of the metal artifacts. In this case, the final reconstruction of the MAPPC algorithm was iterated longer in order to obtain the same spatial and contrast resolution as in the other reconstructions.

Figure 9 shows the reconstructions of a patient with multiple dental fillings. Again all three MAR algorithms reduce the streak artifacts, however the MAPPC algorithm tends to give a better suppression of the artifacts around the teeth and restores more details at a small distance from the artifacts. Figure 9D shows the MAPPC reconstruction when initial and final reconstruction are performed with FBP instead of MLTR.

## VI. Discussion

During the last thirty years, several algorithms were proposed to reduce the artifacts caused by metal implants. None of these algorithms was able to completely eliminate the streak artifacts, to recover all detailed information obscured by the streaks and to produce a diagnostic image fulfilling the high demand on CT image spatial and contrast resolution. It remains a question whether it is possible to find an algorithm that will satisfy these requirements. Especially in the presence of several metallic objects, as can be the case with dental fillings, the task of completely restoring the image becomes very challenging.

In this paper, a new reconstruction procedure for the suppression of metal artifacts was proposed. The core of the MAPPC algorithm is the combination of the creation of an artifact-free constrained image with MAP and completing the projections based on this constrained image. We expected that the use of an image-based projection completion method gives rise to a more consistent sinogram than when interpolation in the sinogram is done. Especially in the case where multiple metallic objects are present, the use of an image-based projection completion method seems superior. There are several parameters in the MAPPC algorithm that need to be tuned. However, all reconstructions have been done with a single set of parameters.

The MAPPC algorithm proposed in this paper was derived from an initial experiment performed to evaluate the effectiveness for metal artifact suppression with iterative reconstruction algorithms. The results showed that neither MLTR nor IMPACT could deal with the metal projections in a correct way and that it may actually be better to ignore them. These findings resulted in the image based projection completion method MAPPC. We believe the major cause for metal artifacts are partial volume effects which explains why neither MLTR nor IMPACT is reducing the artifacts sufficiently. A complete modeling of all the physical properties during reconstruction might result in a full suppression of the metal artifacts.

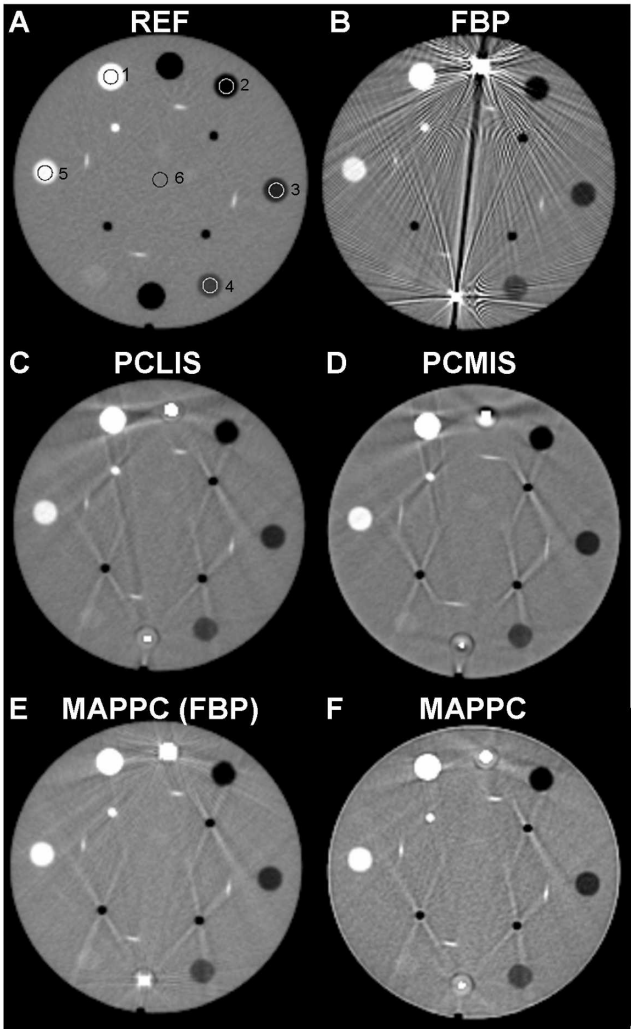


Fig. 7. The reconstructions of module CTP404 of the CATPHAN phantom. The window used was 500 HU centered at 100 HU. A) FBP reconstruction of the phantom without metal inserts. Also shown are the 6 ROIs used in the analysis. The reconstructions of the phantom with metal inserts: B) FBP, C) PCLIS, D) PCMIS, E) MAPPC with the initial and final reconstruction done with FBP, and F) MAPPC.

The MAPPC algorithm performs three iterative reconstructions, which are very time consuming compared to analytical reconstruction. With our (non-optimized) research software, the time needed for the reconstruction of one slice is 1 to 2 minutes on a 3 GHz PC. However, for an algorithm to be useful in daily clinical practice, reconstruction time needs to be limited. In order to speed up the MAPPC algorithm, one can use FBP instead of MLTR for the initial and the final reconstruction, which was shown throughout the results.

The MAPPC algorithm makes use of a multi-modal (absolute intensity) prior. By using such a prior, the MAP reconstruction will tend to attribute one of the modes to each pixel in each iteration. Therefore the use of a multi-modal prior could be seen as a segmentation of the image in different tissue classes. However the difference with a real segmentation is that some variation on the pixel values belonging to the same class is still allowed, especially when the prior is given a low weight. A disadvantage of the multi-modal prior is that

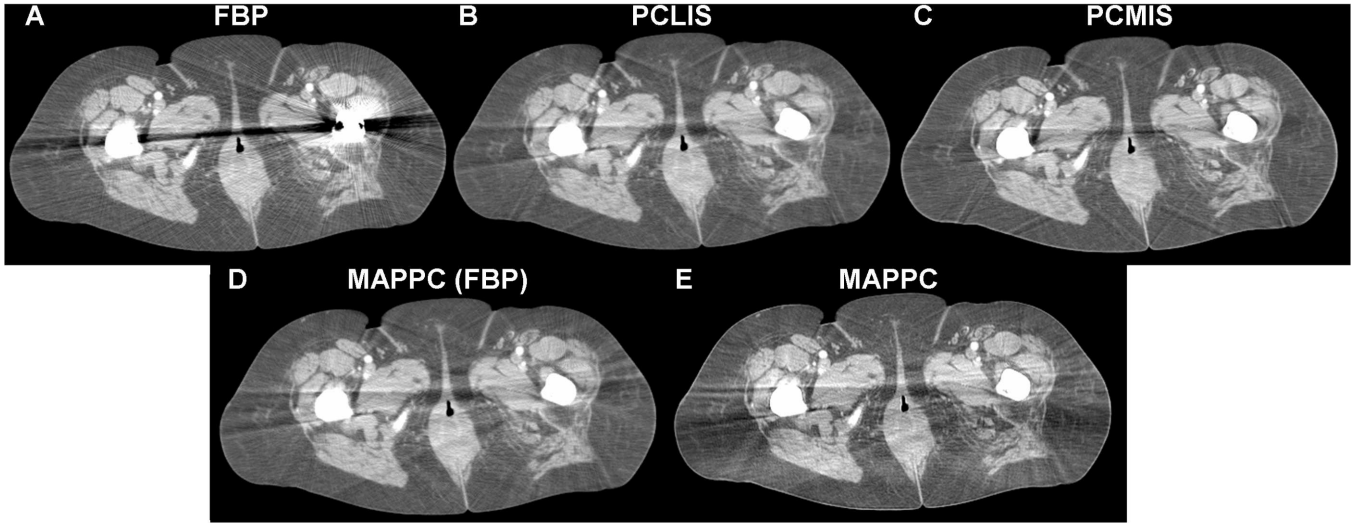


Fig. 8. Reconstructions of a patient with a double hip prosthesis. A) FBP, B) PCLIS, C) PCMIS, D) MAPPC with the initial and final reconstruction performed with FBP, and E) MAPPC. The window used was 400 HU centered at -50 HU.

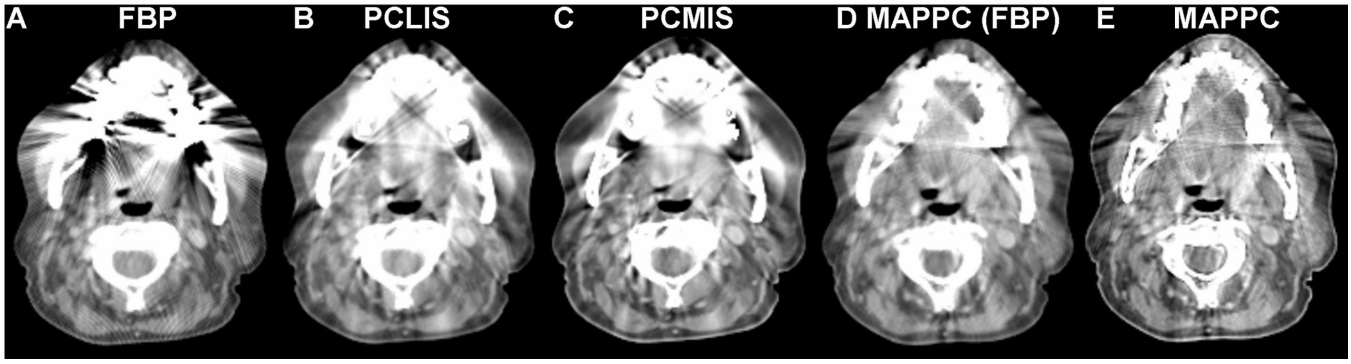


Fig. 9. Reconstructions of a patient with several dental fillings. A) FBP, B) PCLIS, C) PCMIS, D) MAPPC using FBP instead of MLTR for initial and final reconstruction, and E) MAPPC. The window used was 450 HU centered at 0 HU.

it introduces local maxima. The MAPPC algorithm also makes use of the Huber prior. This prior ensures the smoothness of the constrained images. This property turned out to be very beneficial in the case of dental fillings. In addition to this, the Huber prior does not have local maxima, which will improve the convergence of the MAP reconstruction. With this combination of priors we have not observed convergence to an undesired local maximum.

The disadvantage of such a (combination of) prior(s) is that fine details in the image may get lost when the prior is given a high weight. This is in contrast to the aim of recovering as much detail as possible. However, the prior information is only used to produce the constrained image, so the finer details can be recovered during the final reconstruction for which no prior is applied.

To determine the area around the metal pixels, label 1, the initial reconstruction was thresholded for metal. The threshold used was 0.8 $cm^{-1}$. This value was found to result in a good representation of the metal. It is important for the MAPPC algorithm to work that label 1 contains all pixels lying in between different metals and that it also contains all pixels enclosed by the connections lines of the metal pixels. These pixels are defined by the convex hull of the metallic objects The convex hull was further expanded by an amount of 25 pixels for a typical CT reconstruction of 512x512 pixels with a FOV of 500 mm.

The use of projection completion is a popular way to suppress metal artifacts, especially when the metal projections provide no useful information. One of the simplest and best known methods is to use linear interpolation between the nearest neighboring projections unaffected by the metal [4], which was referred to as PCLIS throughout the paper. Here, the results of the simulations, phantom and patient studies were compared with this method. For all cases, the MAPPC gave similar or improved images over PCLIS. For dental fillings, MAPPC systematically outperformed PCLIS. The MAPPC algorithm was also compared to the method of Mahnken et al. [6], referred to as PCMIS. For the phantom measurement and the patient with the double hip prosthesis, PCMIS and MAPPC gave similar results. For the patient with the multiple dental fillings, MAPPC outperformed PCMIS. These results support the remarks made earlier, namely that an image-based projection completion gives rise to a more consistent sinogram and that this is an advantage when multiple metallic objects

are present.

The results of the simulation and phantom experiments show that the use of the MAPPC algorithm improves the images in the presence of metal structures; the CT numbers are restored and details that were obscured by the metal streak artifacts are visualized again. However, as can be seen in the images shown in this paper, the final reconstructions still suffer from small artifacts and have a reduced image contrast when compared to metal-free reconstructions. Further modifications to the MAPPC algorithm could result in improved image spatial and contrast resolution and could reduce these problems. The quality of the constrained image will be a determinating factor for this final image quality. Therefore, further experiments are needed with different priors and prior weights to improve the constrained images. Using a better model of the actual data acquisition, in particular the extension from 2D to 3D cone beam reconstruction, could help to further reduce the metal artifacts and to improve the final image quality. Another possibility to improve the results is the iteration of the MAPPC algorithm.

All results presented in this paper were obtained for a tube voltage of 120 kVp. However, it was verified that the MAPPC algorithm gives quantitative correct results for all voltages used in clinical practice.

A MAR algorithm similar to ours was developed by Bal and Spies [10]. They perform a segmentation of the image, replace the metal with soft tissue and make a forward projection of this modified image. Then they replace the metal projections by the corresponding projections of the segmented image. Reconstruction is done with FBP. However, in the case of strongly distorted images their segmentation is not perfect and black spots remain. Our constrained images do not suffer from this problem because the MAP algorithm was discouraged to create black spots or streaks near the metal by applying a prior with only the modes bone and soft tissue in the surroundings of the metal. However, it must be pointed out that when there are really air pixels in the surroundings of the metal, like it can be the case with dental fillings in the mouth cavity, the algorithm will correctly assign air values to those pixels. In other words, the prior information does not prevail on the information in the data in this case. This is also a characteristic that needs to be taken into account while tuning the weight of the priors. Performing the segmentation during reconstruction gives the MAPPC algorithm two advantages: first, there is a continuous comparison with the original data and, second, by the use of MAP a fuzzy segmentation is obtained.

The method discussed in [17] also combines projection completion with iterative reconstruction. However, they use a sinogram-based interpolation technique to obtain the projected data and then reconstruct these completed data using a weighted MLTR algorithm. The method described in this paper makes use of iterative reconstruction to obtain a constrained image which forms the basis for an image based projection completion. The completed data can then be reconstructed using either FBP or MLTR.

Reduction of the metal artifacts is not only important for the diagnostic value of the CT but also plays a major role in PET/CT. In PET/CT, the CT images are used to derive an attenuation map for the PET data. The artifacts can thus propagate into the PET images disturbing the visual interpretation and influencing the quantitative analysis [1], [2], [29], [30], [31]. It has been shown that the use of a MAR algorithm can eliminate visual artifacts and bias due to metal in the PET images [32]. However in recent studies [33], [34], it was shown that the presence of metallic objects didn't alter the diagnosis made by merely visual means.

In PET/CT, one often does not acquire a full diagnostic CT scan with intravenous and oral contrast. Instead the CT acquisition is only done for the purpose of attenuation correction of the PET. The CT image is then downsampled and smoothed to approximate the resolution of the PET. Then the HU are converted to PET attenuation values with a kVp-dependent scaling method [35]. If the CT is only used for attenuation correction in the presence of metal artifacts, we believe that the constrained image is a sufficiently accurate reconstruction of the attenuation values, the final reconstruction with projection completion is not necessary in this case.

The results in this paper show that the MAPPC algorithm reduces the streak artifacts and restores the CT number of the tissues surrounding the metal. Correct CT numbers are important for radiotherapy treatment planning. If one uses the artifactual FBP reconstructions for treatment planning and no corrections are applied, the electron densities of the tissues shaded by the dark streak artifacts are underestimated, whereas the bright streaks will cause on overestimation of the electron densities. This under- and overestimation will influence the dose calculations for the tumor and the surrounding tissues. Also tumor delineation will become easier with the MAPPC algorithm. However, the MAPPC algorithm will not assign the correct CT number to the metal. To find the correct CT numbers on could use the extended CT-scale [36].

## VII. Conclusion

A new MAR algorithm was proposed that basically consists of two steps: one, the creation of an artifact-free constrained image using a MAP reconstruction procedure, and two, performing projection completion based on this constrained image. Throughout several simulations and a phantom experiment it was shown that the MAPPC algorithm is able to restore the CT numbers in the images and that it recovers details obscured by the metal streak artifacts. However, the MAPPC reconstructions do not fulfill the high standards for CT image spatial and contrast resolution yet. Therefore, investigation is needed to further improve the MAPPC reconstructions.

## VIII. Acknowledgement

The authors thank Karl Stierstorfer and colleagues from Siemens for help with the CT file format and information about the spectrum of the CT scanner, and James Hamill for helpful discussions and good suggestions regarding this paper.

## References

[1] G. W. Goerres, T. F. Hany, E. Kamel et al.,"Head and neck imaging with PET and PET/CT: artefacts from dental implants", *Eur J Nucl Med* vol. 29 (3), 367-370, 2002.

[2] G. W. Goerres, S. I. Ziegler, C. Burger et al., "Artifacts at and PET/CT caused by metallic hip prosthetic material", *Radiology* vol. 226, 577-584, 2003.

[3] R. M. Lewitt and R. H. Bates, "Image reconstruction from projections: III: Projection completion methods (theory)", *Optik*, vol. 50, 189-204, 1978.

[4] W. A. Kalender, R. Hebel and J. Ebersberger, "Reduction of CT artifacts caused by metallic implants", *Radiology*, vol. 164, 576-577, 1987.

[5] G. H. Glover and N. J. Pelc, "An algorithm for the reduction of metal clip artifacts in CT reconstructions", *Med Phys*, vol. 8 (6), 799-807, 1981.

[6] A. H. Mahnken, R. Raupach, J. E. Wildberger et al., "A new algorithm for metal artifact reduction in computed tomography: In vitro and in vivo evaluation after total hip replacement", *Invest Radiol*, vol. 38 (12), 769-775, 2003.

[7] M. Yazdia, L. Gingras and L. Beaulieu,"An adaptive approach to metal artifact reduction in helical computed tomography for radiation therapy treatment planning: experimental and clinical studies", *Int J Radiation Oncology Biol Phys*, vol. 62 (4), 1224-1231, 2005.

[8] O. Watzke and W. A. Kalender, "A pragmatic approach to metal artifact reduction in CT: merging of metal artifact reduced images", *Eur Radiol*, vol. 14, 849-856, 2004.

[9] J. Wei, L. Chen, G. A. Sandison et al.,"X-ray CT high-density artefact suppression in the presence of bones", *Phys Med Biol* vol. 49, 5407 - 5418, 2004.

[10] M. Bal and L. Spies, "Metal artifact reduction in CT using tissue-class modeling and adaptive prefiltering", *Med Phys*, vol. 33 (8), 2852-2859, 2006.

[11] B. De Man, J. Nuyts, P. Dupont et al.,"Metal streak artifacts in X-ray computed tomography: a simulation study",*IEEE Trans Nucl Sci* vol. 46, 691-696, 1999.

[12] J. Nuyts, B. De Man, P. Dupont, et al., "Iterative reconstruction for helical CT: a simulation study", *Phys Med Biol*, vol. 43, 729-737, 1998.

[13] B. De Man, J. Nuyts, P. Dupont et al., "Reduction of metal streak artifacts in x-ray computed tomography using a transmission maximum a posteriori algorithm", *IEEE Trans Nucl Sci*, vol. 47 (3), 977-981, 2000.

[14] C. H. Yan, R. T. Whalen, G. S. Beaupr et al.,"Reconstruction algorithm for polychromatic CT imaging: application to beam hardening correction", *IEEE Trans Med Imaging*, vol. 19 (1), 1-11, 2000.

[15] B. De Man, J. Nuyts, P. Dupont et al., "An iterative maximum-likelihood polychromatic algorithm for CT", *IEEE Trans Med Imaging*, vol. 20 (10), 999-1008, 2001.

[16] I. A. Elbakri and J. A. Fessler, "Segmentation-free statistical image reconstruction for polyenergetic x-ray computed tomography with experimantal validation", *Phys Med Biol* vol. 48, 2453-2477, 2003.

[17] M. Oehler and T. M. Buzug, "Statistical Image Reconstruction for Inconsistent CT Projection Data", *Method Inform Med*, vol. 46 (3), 261-269, 2007.

[18] S. Zhao, D. D. Robertson, G. Wang et al., "X-ray CT metal artifact reduction using wavelets: an application for imaging total hip prostheses", *IEEE Trans Med Imaging*, vol. 19 (12), 1238-1247, 2000.

[19] F. Natterer, *The mathematics of computerized tomography*, New York: Wiley, 1986.

[20] K. Lange and R. Carson, "EM reconstruction algorithms for emission and transmission tomography", *J Comput Assist Tomogr*, vol. 8 (2), 306-16, 1984.

[21] J. Nuyts and S. Stroobants, "Reduction of attenuation correction artifacts in PET-CT", *IEEE NSS-MIC*, proceeding, 2005, 1895-1899.

[22] H. M. Hudson and R. S. Larkin, " Accelerated image reconstruction using ordered subsets of projection data", *IEEE Trans Med Imaging*, vol. 13 (4), 601-609, 1994.

[23] Z. Liang, R. Jaszczak, R. Coleman et al., "Simultaneous reconstruction, segmentation, and edge enhancement of relatively piecewiece continuous images with intensity-level information", *Med Phys*, vol. 18 (3), 394-401, 1991.

[24] J. Nuyts, P. Dupont, S. Stroobants et al., "Simultaneous maximum a posteriori reconstruction of attenuation and activity distributions from emission sinograms", *IEEE Trans Med Imaging*, vol. 18 (5), 393-403, 1999.

[25] S. Geman and D. E. McClure,"Statistical methods for tomographic image reconstruction",*Bull Int Stat Inst* vol. 52 (4), 5-21, 1987.

[26] E. Ü. Mumcuoğlu, R. M. Leahy and S. R. Cherry, "Bayesian reconstruction of PET images: methodology and performance evaluation", *Phys Med Biol*, vol. 41 (9), 1777-1807, 1996.

[27] G. H. Glover, "Compton scatter effects in CT reconstructions", *Med Phys*, vol. 9 (6), 860-867, 1982.

[28] L. Wang, "Cross-Section Reconstruction with a Fan-Beam Scanning Geometry", *IEEE Trans Comput* vol. C-26, 264268, 1977.

[29] E. M. Kamel, C. Burger, A. Buck, et al., "Impact of metallic dental implants on CT-based attenuation correction in a combined PET/CT scanner", *Eur Radiol.* vol. 13, 724-728, 2003.

[30] M. R. AY and H. Zaidi, "Assessment of errors caused by x-ray scatter and use of contrast medium when using CT-based attenuation correction in PET", *Eur J Nucl Med Mol Imaging* vol. 33, 1301-1313, 2006.

[31] C. Lemmens, M-L. Montandon, J. Nuyts, et al., "Impact of Metal Artifacts Due to EEG Electrodes in Brain PET/CT Imaging", Conf. proc. IEEE-MIC, 2007.

[32] K. P. Schäfers, R. Raupach and T. Beyer, "Combined 18F-FDG-PET/CT imaging of the head and neck: An approach to metal artifact correction", *Nuklearmedizin* vol. 45, 219-222, 2006.

[33] D. Faul, C. Lemmens, T. Blodgett, et al., "A clinical investigation of an algorithm for reducing CT image artifacts from dental implants in PET/CT studies", SNM 2007, *J Nucl Med*, vol. 48(Supplement 2), 416P, 2007.

[34] C. Nahmias, C. Lemmens, D. Faul, et al., "Does the reduction in CT images of metal artifacts from dental implants influence the interpretation of the PET images in PET/CT studies of oral/head and neck cancer?", accepted for publication in the *J Nucl Med*

[35] J. P. J. Carney, D. Townsend, V. Rappoport and B. Bendriem, "Method for transforming CT images for attenuation correction in PET/CT imaging", *Med Phys* vol. 33:976-983, 2006.

[36] C. Coolens and P. J. Childs, "Calibration of CT Hounsfield units for radiotherapy treatment planning of patients with metallic hip prostheses: the use of the extended CT-scale", *Phys Med Biol*, vol. 48, 1591-1603, 2003.